Activity report of the Italian CRG beamline at the European Synchrotron Radiation Facility (ESRF)

N. 7 - December 2019

Grenoble, December 2019

Responsabile editoriale: Francesco d'Acapito
(*dacapito@iom.cnr.it*)

Editing: Roberta De Donatis
(*roberta.dedonatis@cnr.it*)

ISSN 2553-9248

LISA

Annual Report 2019

Istituto Officina dei Materiali

Abstract

This document resumes the activity of the Italian CRG beamline at ESRF (LISA project) during year 2019. The latest news from the beamline are presented as well as details on the technical activity, highlight experiments and publications.

Keywords

Italian beamline at ESRF, BM08

LISA project

X-ray Absorption Spectroscopy

Index

1. Foreword

This year has been particularly quiet at LISA, with the ESRF storage ring shut down due to the works for EBS. Nonetheless, the beamline staff has been very active as in May 2019 we underwent the periodic review from the Beamline Review Panel (BLRP) appointed by ESRF. For this, a report has been prepared describing the beamline activity during the last 5 years and the document has been published as a special issue of the annual reports in the IOM repository (https://www.iom.cnr.it/gilda-reports). The BLRP has appreciated the renewal works carried out so far and has expressed a positive opinion about the renewal of the Operation Contract. Concerning the submission of proposal there will be no changes from the point of view of ESRF quota, the next deadline being announced for Mar 2nd 2020. For the CRG quota: details will be defined and circulated in the forthcoming weeks but the aim is to keep the usual deadline beginning of May. The beamline is expected to resume full operation during May 2020 followed by two months of tests whereas the official user mode will resume by end of August 2020.

The technical activity on the instrument has been concentrated on the realignment of the whole beamline because the new beam from EBS is displaced of about 3mrad outwards respect to that of ESRF. This means a horizontal movement of the whole beamline: about 60 mm at the Front End and 150 mm at the sample position. All the vacuum vessels have been displaced consequently as described in Section 1.2. For the same reason the lead hutches need to be modified: the drawings have been prepared and the intervention is scheduled for the first months of year 2020. Concerning the activity about software it is worth to remind that in the forthcoming years the old beamline control environment “SPEC” will be abandoned and a new environment called “BLISS” will be adopted. At present we are carrying out some preparatory works aimed to the shift as described in Section 2.2.

Concerning events that have involved the LISA staff we recall here the visit from students of the local Cité Scolaire Internationale (appeared in the CNR news https://www.cnr.it/it/news/8605) and the organization of the international school on “How to assess the structure of glasses” in collaboration with CNRS and USTV (https://www.cnr.it/it/news/9079) that was attended by about 70 participants, students and young researchers from academia and industry.
For year 2020 we are organizing a satellite event at the SILS meeting 2020 dedicated to LISA and its activities with the new EBS source. Details on the event will be published soon. The event will take place on July 1st in Bologna (https://eventi.unibo.it/sils-2020): mark you agendas !

Two words about people with a thought to our colleague Aleksander “Sandi” de Luisa who played a pivotal role in the design of LISA and prematurely passed away on June 1st 2019. And all the best to Giovanni Orazio Lepore who, after 4 years spent at LISA as staff, got a researcher position at the Florence University. Looking forward to see you here again as an ‘experienced user’.

F. d’Acapito

2.1. Interventions on infrastructures

G. O. Lepore, F. d'Acapito (CNR-IOM, Grenoble)

For the future EBS ring, LISA will make use of the Single Bend Magnet (SBM) with a magnetic field of 0.85 T, thus keeping the same previous critical energy. In order to exploit the new source, it has been necessary to realign all the beamline equipment, including optical elements, by several tens of millimetres. The intervention required the installation of an adaptation flange prior to the RV0 valve (Figure 1, left) to accommodate the horizontal drift of the future beam and the realignment of the beamline optical elements and experimental end stations. The repositioning of the optical elements was extremely delicate since, given the future position of the beam, the necessary movements ranged from ≈60 mm at the front end to ≈150 mm at the experimental end station in the second hutch (Figure 1 Right); on top of that, all optical elements had to be vented in dry nitrogen and then be put back in high vacuum.

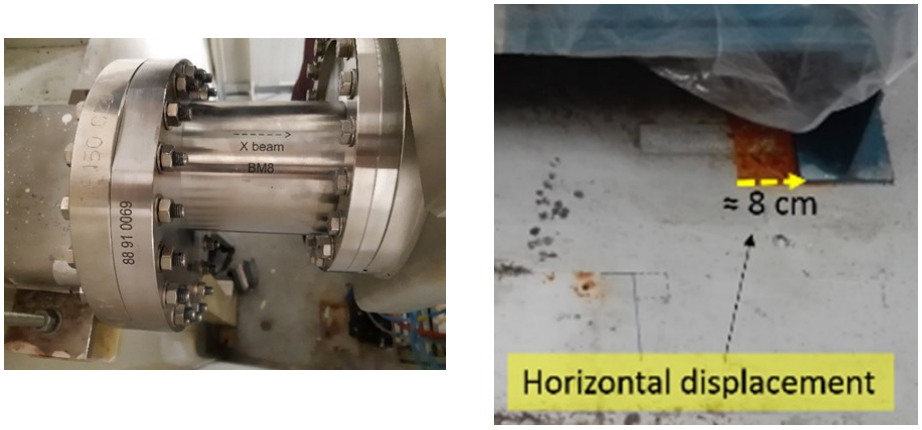

Figure 1: Left) the adaptation flange installed just after the Front End and before the first beamline gate valve (RV0). Right) Detail of the base of the second mirror with the displacement evidenced on the floor.

The realignment of the beamline has been successfully performed by the beamline staff, together with M. Hahn and E. Dettona from the ESRF-CRG group, N. Levet from the ESRF Alignment and Geodesy group and the staff of the CIC ORIO Company. Another intervention linked to the new position of the EBS beam consists in the modification of the lead shielding in order to correctly position the transfer pipe. This intervention affected the entrance and/or exit of the various hutches and involved the dismounting of the previous installations (transfer pipes and radiation shielding). The final works will be carried out in the first months of year 2020.

Finally, a new fence has been installed outside the Optic Hutch for reasons linked to radioprotection for the new ring (Figure 2).

Figure 2: Left: The new fence contouring the Optic Hutch. Right: The lead shielding at the entrance of EH2 ready to be modified to allocate the transfer pipe in the new position.

2.2. Farewell SPEC, welcome BLISS

A. Puri (CNR-IOM, Grenoble)

The BeamLine Instrumentation Support Software (BLISS) is the new beamline control system, substituting SPEC, currently under development at ESRF, with a full deployment planned for the end of the EBS upgrade program in 2022. BLISS provides a global approach to conduct synchrotron experiments, where is required to synchronously control motors, detectors and various acquisition devices, thanks to hardware integration, Python sequences and an advanced scanning engine. Very similar to a Python package, BLISS can be easily embedded in any Python application and its data management features enable online data analysis. In addition, BLISS provides tools to enhance scientist user experience and facilitate integration on ESRF beamlines.

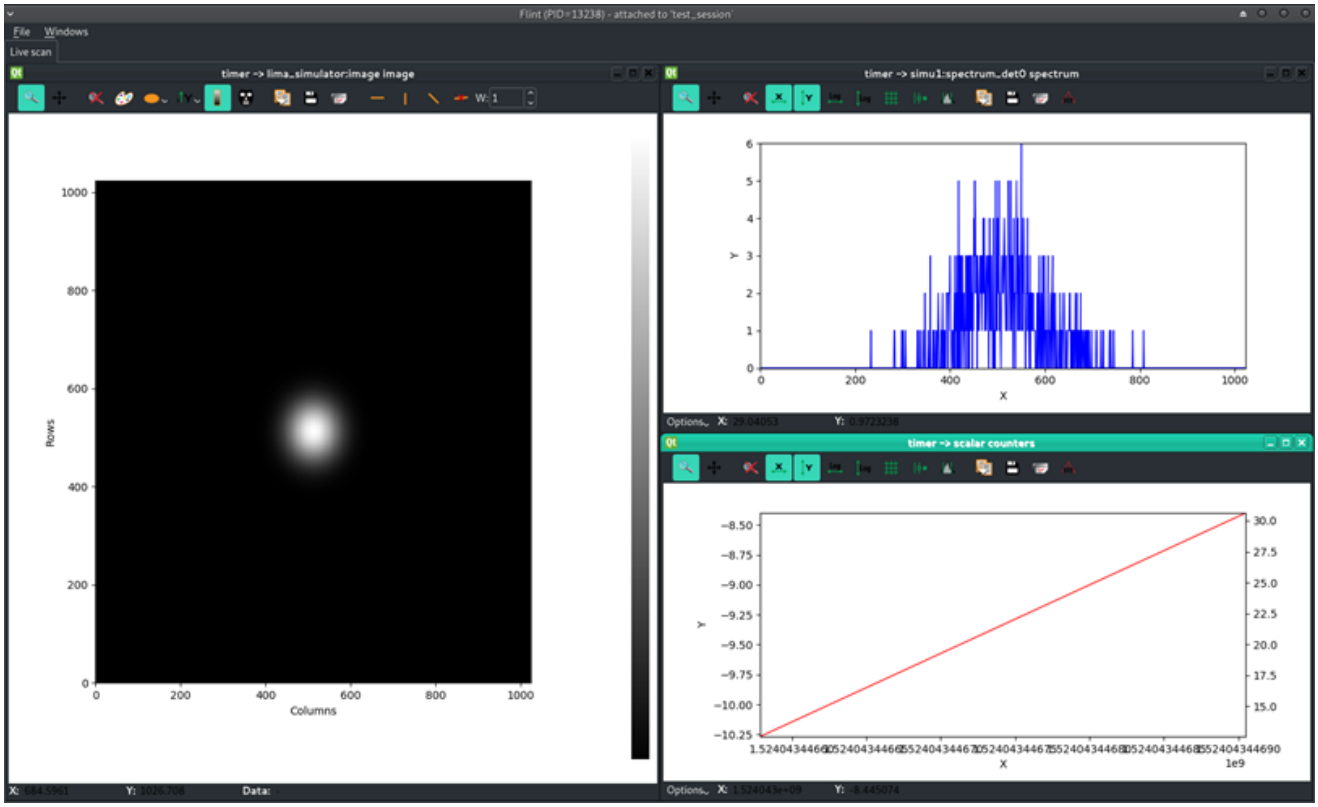

Figure 3: Example of data visualisation in BLISS using the FLINT application.

At present BLISS testing is underway at LISA to check the compatibility with the instrumentation of the beamline. BLISS has been successfully installed on a test machine and a first test session has been created. Further tests to verify the correct motor movements will be carried out soon. Although the beamline will continue to use SPEC during the restart period, a complete migration to BLISS is foreseen in a couple of years. The beamline staff wish to thank M. Rovezzi (CNRS-FAME beamline) for the support during the first BLISS tests.

3.1.

Unveiling the mechanism behind Ovonic Threshold Switching in chalcogenide glasses used in ultimate non-volatile resistive memories

P. Noé[1,], A. Verdy[1], F. d'Acapito[2], J.-B. Dory[1], J.-B. Jager[3], J. Gaudin[4] and J.-Y. Raty[1,5,*]*

[1]CEA, LETI F-38000 Grenoble, France, [2]CNR-IOM-OGG c/o ESRF, F-38043 Grenoble, France, [3]CEA, IRIG F-38000 Grenoble, France, [4]CELIA, F-33405 Talence, France, [5]FNRS, Université de Liège, B4000 Sart-Tilman, Belgium.

The unique phenomenon called OTS (Ovonic Threshold Switching) observed in some Se and Te-based chalcogenide glasses has recently led to a major technological breakthrough in the field of memories. Indeed, it has enabled the advent of high-density 3D non-volatile resistive memories thanks to the combination of a phase-change memory (PCM) element and an OTS selector, both based on a chalcogenide material. This opens the way to storage class memories (SCM) and innovative brain-inspired neuromorphic circuits. However, fifty years after its discovery, the origin of the OTS effect, which is a unique non-linear conductivity behavior observed in some chalcogenide glasses during the application of high electric fields was still not explained or fully understood.

In the present study, we have elucidated the mechanism behind OTS switching by means of new state-of-the-art OTS materials using electrical, optical and X-ray absorption spectroscopy (XAS) experiments as well as *ab initio* molecular dynamics (AIMD) simulations. First, by coupling the analysis of the electronic properties and behavior of OTS films in selector devices with the study of the amorphous structure, we were able to establish design rules to further optimize the OTS properties of amorphous chalcogenides. For example, controlling the number of homopolar or wrong bonds is a key parameter to limit the leakage current below the threshold. The latter is the main limit to the increase of the size of the crossbar arrays in 3D memory devices. Besides, the control of the material bandgap allows to adjust the value of the threshold voltage V_{th}. In addition, increasing the stiffness of the amorphous by introducing covalent bonding elements such as N atoms improves the stability of the amorphous phase against crystallization and thus the endurance of the OTS selector. Finally, while the subthreshold conduction mechanisms in chalcogenide glasses are now well understood thanks to increasingly accurate models to describe experimental observations, the underlying physical mechanism involved in OTS switching is still much debated. Using EXAFS (Extended X-ray Absorption Fine Structure) data acquired at the Ge, Sb and Se K-edges of GeSe-based OTS glasses on the LISA beamline, we were able to build robust structural models of prototypical OTS glasses in order to simulate the impact of electrical field application on the OTS material by means of advanced AIMD simulations (Figure 4).

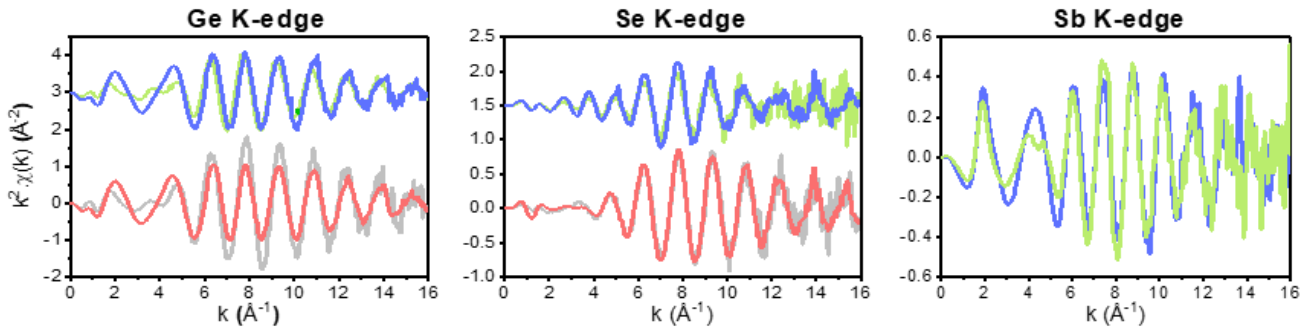

Figure 4: Analysis of the local structure of GeSe-based OTS thin films by means of XAS experiment with experimental EXAFS spectra obtained at the Ge, Se and Sb K-edges for the 4 prototypical GeSe(Sb, N) OTS thin film samples.

Successively, advanced AIMD simulation was used to link the OTS mechanism to subtle structural rearrangements of the amorphous phase during the application of high electric fields (figure 5).

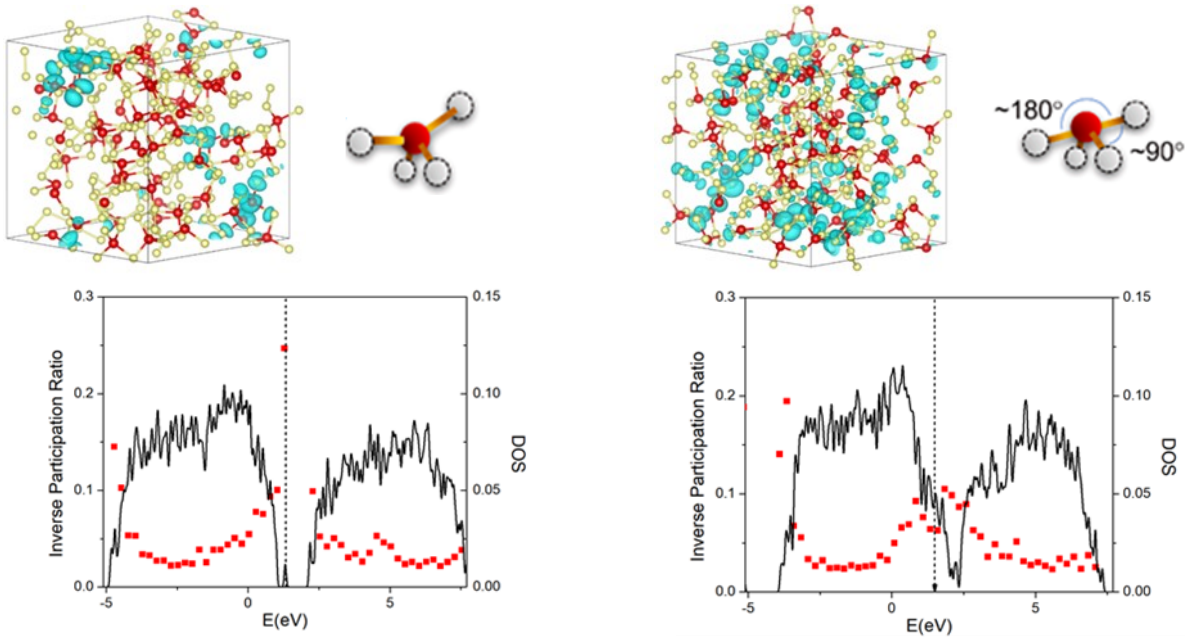

Figure 5. Instantaneous snapshots of the electronic density at the Fermi energy (Ge: red; Se: yellow) as well as eDoS for amorphous $Ge_{30}Se_{70}$ OTS model in (left) the pristine and (right) excited state. The initial semiconducting material has a large bandgap (the Fermi level is indicated by the dashed line) with some localized defects states and band-tails as evidenced by plotting the Inverse Participation Ratio (IPR, shown by the red dots). In the metallic excited state, as the bandgap closes the DoS increases strongly and the IPR values drop around the Fermi level. The delocalization of states indicated by this drop in IPR value around E_F is illustrated on the atomic snapshots in which the electronic Kohn-Sham states at the Fermi level are plotted as blue iso-surface curves (drawn at 15% of their maximal value). A strong localization of electrons is observed in the initial insulating state (left) by opposite to the generalized electronic delocalization visible in the excited state (right). The huge increase of conductivity upon electric field application observed at threshold switching in OTS materials can then be explained by the strong delocalization of the electronic states around E_F. Although the global topology of the network is conserved upon excitation, important changes can be observed on the proportion of quasi-aligned bonds upon excitation giving rise to structural motifs reminiscent to metavalent bonds as illustrated for instance by means of balls&sticks molecules showing structural changes occurring around Ge atoms upon OTS switching.

In particular, the excitation of glasses under a high electric field leads to the alignment of certain bonds (see e.g. molecules displayed as insets in figure 2) and the appearance of local structural patterns reminiscent of the new metavalent bond (MVB) recently described in crystalline phase of chalcogenide-based phase-change materials [1, 2]. Such MVB are thus responsible for a huge change in electronic Density of States (eDoS) accompanied by a drop in the electronic conductivity of the materials. In addition, our current OTS switching model tends to establish for the first time the common link between chalcogenide materials belonging to the phase-change materials and those of the OTS family. In both systems, the MVB mechanism is responsible for the unique properties that led to the recent breakthrough in non-volatile memories by coupling a PCM resistive cell and an OTS selector. As shown here, the main difference between PCM and OTS materials lies in their ability to stabilize the MVB mechanism and in the energy barrier to crystallization.

Publication: [Science Advances (2020), in press, DOI: 10.1126/sciadv.aay2830]

References: [1] Wuttig, et al., J.-Y. *Advanced Materials* **30**, 1803777 (2018); [2] Raty, J.-Y. *et al. Advanced Materials* **31**, 1806280 (2019).

Black Phosphorus/Palladium Nanohybrid: Unraveling the Nature of P–Pd Interaction and Application in Selective Hydrogenation

M.Vanni,[1,2] M.Serrano-Ruiz,[1] F.Telesio,[3] S.Heun,[3] M.Banchelli,[4] P.Matteini,[4] A.M.Mio,[5] G.Nicotra,[5] C.Spinella,[5] S. Caporali,[6] A.Giaccherini,[6] F. d'Acapito,[7] M.Caporali,[1] and M.Peruzzini[1]

[1]CNR-ICCOM Florence, [2]University of Siena, [3]NEST Pisa, [4]CNR-IFAC Florence, [5]CNR-IMM Catania, [6]University of Florence, [7]CNR-IOM-OGG Grenoble

The science of 2D materials has grown dramatically during the last fifteen years. Black phosphorus (bP), in particular, aroused great excitement because of its unique physicochemical properties. The structure of bP resembles the honeycomb motif of graphene. However, due to a different orbital hybridization, these rings adopt a chair conformation and each phosphorus atom is bearing a lone-pair that can get involved in bonds with metal fragments. These features make 2D bP a suitable platform to anchor metal nanoparticles (M NPs) and many examples of M NPs/ bP heterostructures have already been reported. However, minor attention has been devoted to shed light on the nature of the interaction between bP and metals. A new Pd/bP nanohybrid was prepared with an *in situ* reduction process growing Pd NPs (~ 3 nm, see Figure 6 Left) directly above the surface of 2D bP.

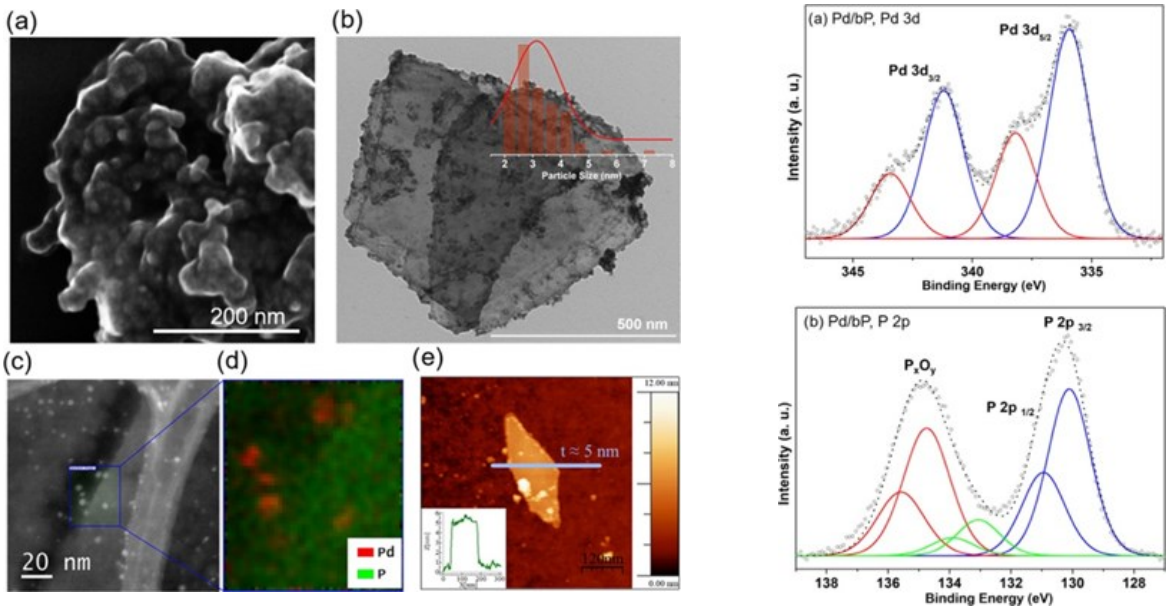

Figure 6: Left: (a) SEM and (b) TEM image of Pd/bP with relative size distribution. (c) HAADF STEM image of Pd/bP on a lacey carbon grid and (d) elemental mapping of the selected area. (e) AFM image of a Pd/bP flake on Si/SiO_2. Right: (a) Pd 3d and (b) P 2p core-level XPS spectra of Pd/bP.

XPS measurements carried out on the nanohybrid revealed that, beside bulk metallic Pd(0), an electrodepleted palladium species was present, probably in oxidation state +2 (see Figure 6 Right). This was attributed to Pd–P bonds between the surface Pd atoms of the nanoparticles and bP. EXAFS measurements at the Pd K-edge were carried out at the beamline LISA (ESRF) on Pd/bP and on the following materials taken as standards: PdO, Pd NPs capped with the phosphine ligand PTA and labelled as Pd@PTA, palladium phosphide nanoparticles PdP_2 NPs, Pd NPs supported on carbon Pd/C, and Pd metal foil. The raw EXFAS spectra and the corresponding Fourier transforms are shown in Figure 7.

From the spectra two distinct bond distances were identified in sample Pd/bP. One corresponded to Pd–Pd bonds. The other, which could be fitted only using P ligands for Pd, could be safely attributed to Pd–P bonds, in agreement with the XPS observation. The measured Pd–P distance was only 2.26(3) Å, indicating a very strong interaction between phosphorus and palladium. Remarkably, the reference sample Pd@PTA exhibited Pd–P = 2.25 Å, which was consistent with the bond distance Pd–P found in some coordination compounds such as $[Pd(PTAH)_4]^{4+}$.

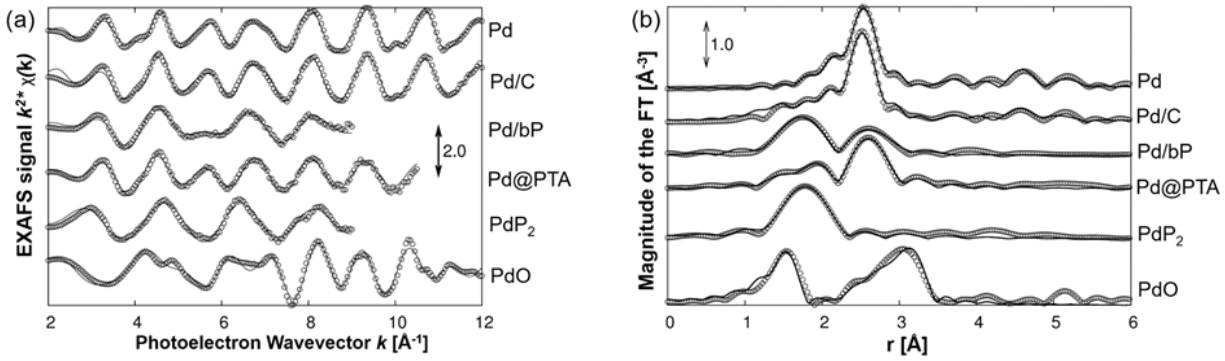

Figure 7: (a) EXAFS data at the Pd K-edge and (b) the corresponding Fourier transforms.

These findings provided the first experimental evidence that bP is able to form strong coordinative bonds of covalent nature with transition metals. The Pd/bP nanohybrid was also used successfully as a catalyst in the hydrogenation of chloronitrobenzene to chloroaniline. The latter is a valuable synthetic intermediate in many industrial processes. The mechanical stabilization imparted to the catalyst by the strong Pd–P bond and the synergic effect of palladium and bP made it possible to carry out the hydrogenation with excellent selectivity.

Publication: [*Chem. Mater.* **31** (2019), 5075.]

Chemical variability of artificial stone powders in relation to their health effects

F. Di Benedetto[1], A. Giaccherini[1], G. Montegrossi[2], L.A. Pardi[3], A. Zoleo[4], F. Capolupo [5], M. Innocenti[5], G.O. Lepore[6], F. d'Acapito[6], F. Capacci[7], C. Poli[7], T.E. Iaia[7], A. Buccianti [1] and M. Romanelli[1]

[1]Dip. Scienze della Terra, Univ. Firenze, Italy. [2]CNR – Ist. Geoscienze e Georisorse, Firenze, Italy. [3]CNR – Ist. Processi Chimico Fisici, Italy. [4]Dip. Scienze Chimiche, Univ. Padova, Italy. [5]Dip. Chimica, Univ. Firenze, Italy. [6]CNR – Ist. Officina dei Materiali - OGG c/o, ESRF, France. [7]Dip. Prevenzione, PISLL, Health Agency of Tuscany, Italy.

Artificial stone (AS) is a composite material realised assembling powders, and sometimes fragments, of natural stones with a binder. A common assemblage adopts unsaturated polyester resins as binder, and crystalline silica (CS) as stone. Numerous products (as e.g. countertops or sanitary furniture) are realised with this composite.
Numerous diseases among the AS workers (ASW), often characterised by short latency and high severity, were described, following the commercial diffusion of AS [1]. However, a straightforward relationship of such response with the workers' exposure could not be found. Many factors may contribute to the toxicity of such systems. Among them, we must consider the presence of transition metal ions (mainly Fe) and radicals at the AS surface, coupled to eventual surface alteration resulting from the mechanical treatments.
The interaction between respirable crystalline silica and the resin was pointed out by experimental studies [2] that highlighted the resin's capability to provide a coating film over the mineral surfaces during the countertops finishing procedures. In order to further understand chemical and physico-chemical changes occurring during industrial processing, a new experimental study was carried out on raw and processed (under wet and dry polishing) industrial AS stones by means of SEM, XRPD, XRF, XAS and continuous wave (cw) and pulsed Electron Paramagnetic Resonance (EPR) spectroscopy.
The study showed that, in all the samples, the powders are constituted by either quartz (qz) or cristobalite (cb) as major CS components and only minor mineralogical phases as accessory components. No chemical fingerprints associated to qz- or cb-bearing samples was highlighted, despite the extremely variable chemical composition of the natural powders forming the AS. On the other hand, a detailed statistical analysis, aimed to ascertain natural chemical associations, pointed out the presence of a clear chemical fingerprint discriminating raw from processed samples, and wet from dry processed samples.
EXAFS analyses confirm this feature, showing that in both wet and dry processing, contamination by metallic Fe (likely provided by working tools) occurs (Figure 8 Left). Moreover, the modifications induced by the mechanical treatments extend to all the detected Fe forms by modifying Fe coordination and/or Fe oxidation state. The EPR (cw and pulsed) study allowed to observe the presence of additional radicals in both the dry- and wet-processed samples (Figure 8, Right). Distinct additional radical species (mainly of the Si× type) were identified in qz- and cb-bearing samples, while no changes associated to the type of processing were found.

In summary, the multimethodic approach of this study pointed out that:
(1) a specific chemical contamination of the parent AS occurs on the basis of the wet or dry processing;
(2) the processing of AS results in detectable changes of the Fe speciation;
(3) unusually high levels of cristobalite, whose toxicity is considered even higher than that of quartz, were detected.

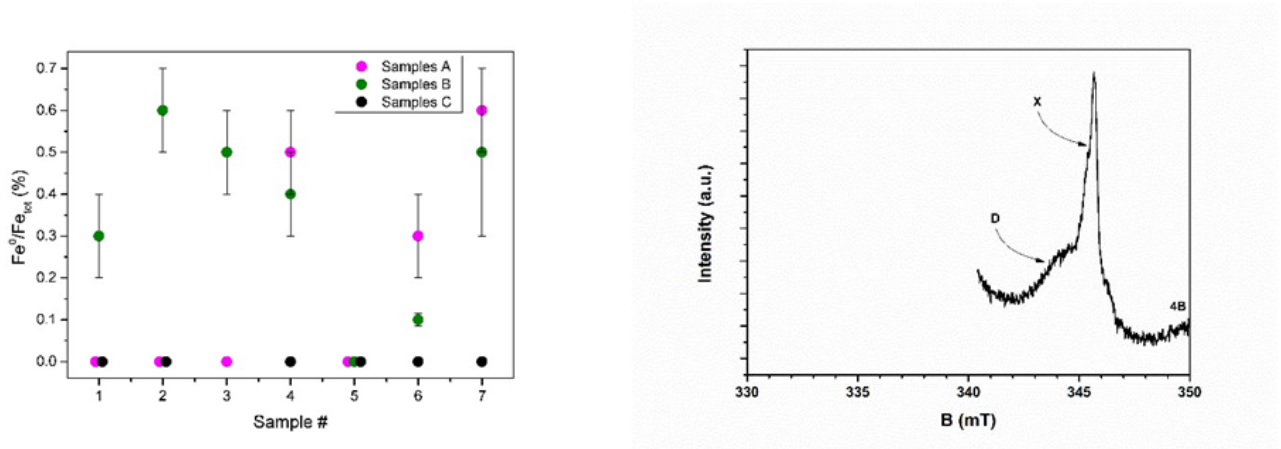

Figure *8: Left, ratio between metallic and total Fe content (Fe0/Fetot) evaluated from EXAFS data analysis. Right, exemplar EPR spectrum of a sample were the additional radical species is highlighted.*

A definite change in radical speciation is operated by AS processing. The long life of the additional species is in favour of an active role of protection played by the resin, in agreement with [2]. Since redox and toxic species are involved, the active mechanisms of dust contamination are highly relevant for toxicity studies.
A distinct behaviour of these materials can thus be deduced. This involves a coupled effect of chemical contamination and thermo-mechanical processes able to modify the chemical and physico-chemical features of the parent materials. This in turn may lead to differentiated types of exposure for AS workers operating the dry or the wet polishing.

Publication: [Sci. Rep. 9, 6531 (2019); doi: 10.1038/s41598-019-42238-2.]

References: [1] R.F. Hoy, et al., Occup. Environ. Med. 75, 3–5 (2018); [2] C. Pavan, et al., Toxicol. Sci. 153, 4–17 (2016).

Operando X-ray absorption spectroscopy of WO_3 photoanodes

M. Fracchia [1], V. Cristino[2], A. Vertova,[3,4], S. Rondinini[3,4], S. Caramori[2], P. Ghigna[1], A. Minguzzi[3,4]

[1]Department of Chemistry, University of Pavia, [2]Department of Chemical and Pharmaceutical Sciences, University of Ferrara, [3]Deparment of Chemistry, University of Milan, [4]INSTM (Istituto Nazionale di Scienza e Tecnologia dei Materiali), Florence

In the recent years, photocatalytic water splitting has attracted a lot of attention as a promising and sustainable way to produce H_2, a clean energy vector, by exploitation of the solar energy. In this process, a semiconductor employed as photoanode or photocathode is coupled to a counter electrode and illuminated with the solar light. Light absorption leads to the photogeneration of electron/hole pairs, which drive the water splitting reaction. If the semiconductor is employed as photoanode, the photogenerated electrons are driven to the counter-electrode, while the holes are responsible for the oxidation of water to form O_2. The kinetics associated to this reaction is sluggish, since it requires the simultaneous transfer of four electrons. Moreover, the photogenerated carriers can undergo processes of recombination and/or trapping at the surface states, thus decreasing the efficiency of the process. It has therefore emerged the urgency to find adequate techniques to monitor the fate of the photogenerated carriers and to study the mechanism of the photocatalytic water splitting, with the final aim of rationally design appropriate tailored materials for this reaction.

Operando X-ray Absorption Spectroscopy (XAS) proved to be particularly suitable for this purpose, since it is highly informative and versatile, thus allowing investigation of a photocathode or photoanode under realistic conditions of operation. In this work, WO_3 photoanodes, which are among the most employed semiconductors for water splitting, were investigated through operando XAS, using a properly-designed three-electrode spectroelectrochemical cell (1), in aqueous Na_2SO_4 (0.1 M). The XAS spectra were acquired in fluorescence mode at the W L_{III} edge, coupling spectroscopic measurements to electrochemical techniques. Two main approaches were followed: i) the acquisition of differential spectra Δμ: for each photon energy, the acquisition is performed both in dark and under illumination, thus minimizing the systematic errors. This allows to immediately compare the two spectra, searching for variations induced by illumination; ii) the use of an approach similar to fixed-energy X-ray absorption voltammetry (FEXRAV) (2): the energy is kept constant at a value where there is a high contrast of μ of different standard phases; the absorption coefficient is then measured at this energy and at a fixed potential, while switching on and off the light.

The results of the first approach are shown in Figure 9a. The spectrum of WO_3 is shown by the blue line in the upper panel: its white line has a characteristic splitting, due to the transition from the filled 2*p* orbitals to empty 5*d* states, split by the crystal field into states of t_{2g} (at lower energies) and e_g (at higher energies) symmetry. The two corresponding energies are marked by the dashed lines. The difference spectrum (light minus dark) obtained at open circuit potential (OCP) is negative in correspondence of the t_{2g} orbitals only; this can be attributed to the injection of electrons into these orbitals as a consequence of photoexcitation. When a potential is applied (0.35 V vs RHE) the Δμ signal is flat: in fact, electrons and holes are rapidly swept to the counter electrode or to the electrolytic solution.

With the second approach, μ was measured at OCP in correspondence of the t_{2g} (Figure 9 b) and e_g orbitals (Figure 9 c) while switching on and off the light. In correspondence of the t_{2g} energy, when the light is switched on, μ has a sharp decrease due to the injection of the electrons in these states. On the contrary, the same plot at the e_g energy shows only the increasing trend of μ, thus demonstrating that no direct injection occurs in these orbitals. The FEXRAV gives also interesting information about the long-term behaviour of the material, showing a progressive increase of μ, due to various possible underlying processes.

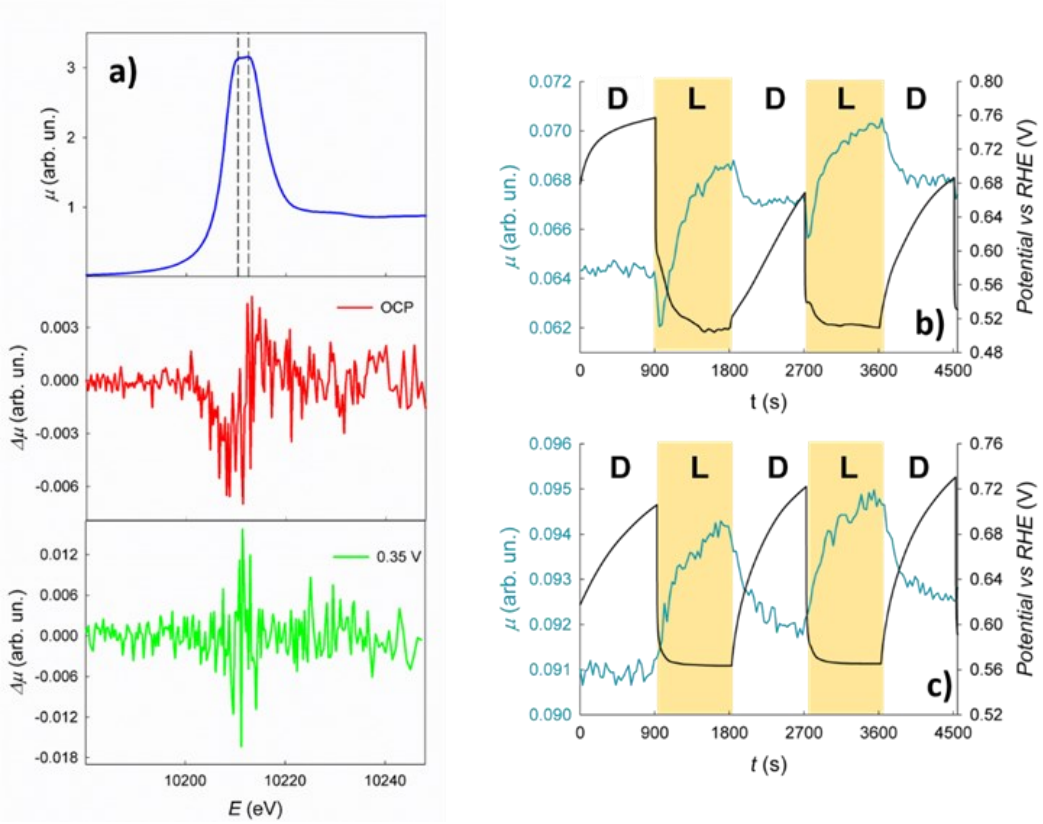

Figure 9 a) Δμ spectra at the W LIII-edge at OCP (red curve) and at 0.35 V (green curve). The blue curve in the upper panel shows the XANES spectrum of WO3, where the dashed lines are in correspondence of the energy of the t2g and eg orbitals. b) Fixed energy X-ray absorption coefficient plotted as a function of time at the energy of the t_{2g} and c) e_g orbitals. Right, black axes: open circuit potential.

Publication: [Electrochim. Acta **320** (2019), 134561.]

References: (1) E. Achilli *et al.*, J. Synchrotron Radiat. **23** (2016), 622-628; (2) A. Minguzzi *et al.*, Anal. Chem. **85** (2013), 7009-7013.

Coupling oxyanions (As) transformation with Fe and S cycling under redox oscillations

V. T.H. Phan[1], R.-M. Couture[2], F. Bardelli[3], R. Bernier-Latmani[4], L. Charlet[5]

[1]IPAG, UGA, 38400, France, Département de Chimie, [2]Université Laval, Québec, Canada, [3]Institute of Nanotechnology (CNR-Nanotec), 00186 Rome, Italy, [4]EPFL, Lausanne, Switzerland, [5]ISTerre, UGA, 38400, France

Sub-surface biogeochemical systems can oscillate between oxic and anoxic conditions. Cumulative effects of such periodic redox cycling on the mobility, speciation and toxicity of As and Se in the Fe-S-C system in alluvial sediment (Mekong Delta, Vietnam) were investigated using a batch bioreactor system imposing successive half-cycles of oxidizing and reducing conditions. Contrasting sediments were subjected to this treatment: S1 contained high pyrite (FeS_2) content; S2 contained both pyrite (FeS_2) and gypsum ($CaSO_4$), S3 contained low FeS_2, but high organic matter (NOM) and sulfate (SO_4^{2-}).

Reduced – oxidized oscillations were carried out by automatically modulating the influx gas between the mixture of N_2 and 300 ppm CO_2 in anoxic half-cycle (7 days) except for the first one with 5 days, and compressed air of 1% CO_2, 79% N_2 and 20% O_2 in oxic half-cycle (7 days) using an Agilent switching unit and a system of solenoid valves. Redox cycles were monitored for approximately 42 days. Three batch bioreactors, S1, S3 and S2, were prepared with 1L of sediment suspension containing 100g of dry sediment and the different contaminants including: (S1) 100g of 14 m, high pyrite and no gypsum + 1L H_2O + 50µM $NaAsO_2$ + 8.33 mM OC (cellobiose) + 0.1 mM of Na_2SO_4; (S2) 100g of 7 m, high pyrite and gypsum + 1L H_2O + 50µM $NaAsO_3$ + 8.33 mM OC (cellobiose) + 0.1 mM of Na_2SO_4 and (S3) 100g of 16 m, low pyrite and high organic matter (OM) + 1L H_2O + 50µM $NaAsO_2$ + 8.33 mM OC (cellobiose) + 0.1 mM of Na_2SO_4. The E_h and pH data were recorded automatically every 10 s using an Aligent 34970A Bench Link Data Logger through the E_h and pH electrodes (Mettler-Toledo Xerolyt Solid). The aqueous phase, including trace and major cations, major anions, DOC, As species (As(III), As(V), MMA and DMA) were analyzed using ICP-OES, IC, TOC, HPLC-ICP-MS, respectively. Solid-phase samples were collected from the two reactors at the end of the redox cycles. X-ray absorption near edge structure (XANES) was used to characterize both As at the bending magnet beamline BM08-LISA of the European Synchrotron Radiation Facility (France) and S speciation at the XAFS beamline of the Elettra synchrotron (Italy).

The analytical results of pore water and microbial analysis in reactor S1 suggest the pyrite oxidation was observed during the oxic conditions, either by Fe^{3+} or O_2 along with the release of SO_4^{2-} and a lower of pH (3 - 4). This was not observed during anoxic condition due to the absence of SRB. About 90% of As was absorbed during oxic conditions, but released back to the aqueous phase cycle after cycle. In reactor S2, the increase of dissolved Ca^{2+} and SO_4^{2-} is likely related both gypsum dissolution and also pyrite oxidation, possibly followed by the formation of schwertmannite. The $As_{(aq)}$ concentrations was fluctuated in the first two cycles, then was sequestered in the last cycle via Fe (oxyhydr)oxides and hydroxysulfates (e.g. schwertmannites). While in the reactor 3, we observed Fe and SO_4^{2-} reduction in anoxic, Fe^{2+} and S(-II) oxidation in oxic conditions and As was immobilized during the oxic cycles. After an initial release during the first anoxic half-cycle it was increasingly sequester even along subsequent anoxic cycles (Figure 10)

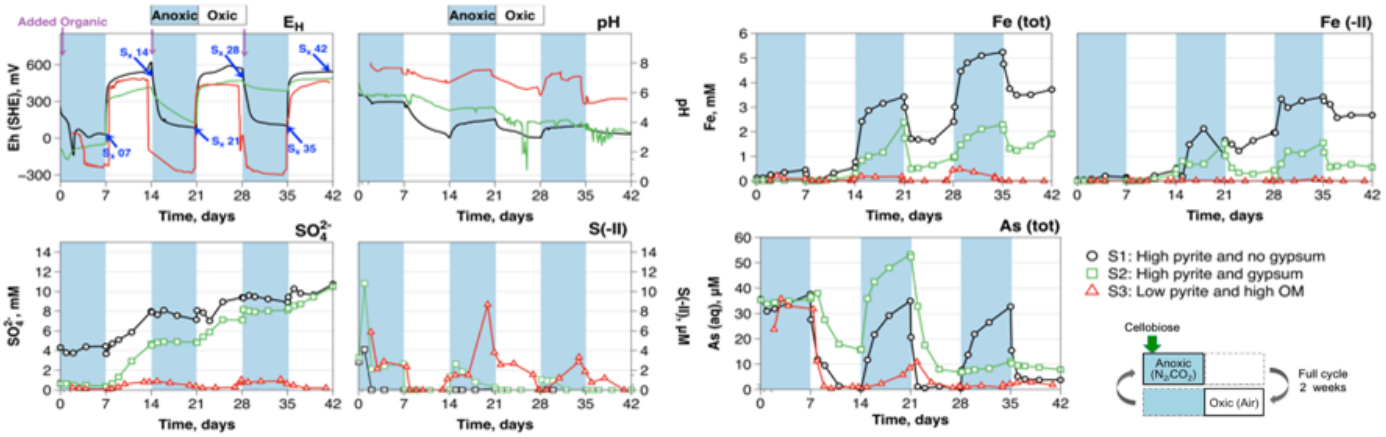

Figure 10 Aqueous measured Eh(SHE), Fe(tot), Fe (-II), SO42-, S(-II) and As(tot) in function of time in sediment suspension of S1, S2 and S3. Sampling point for As K-edge XANES are shown on the Eh graph with the blue arrow in the end of each half-cycle.

Together with the results of solid phase, change in As mobility and cumulative changes in the substrate along redox cycles were expected due to the evolution of mineral assemblages. In the reactor S1, Fe and As were mobilized under anoxic conditions and replenished at every oxic half-cycle. Remobilization proceed along with the pyrite oxidation, a lowering of the pH value and apparent inhibition of microbial sulfate reduction. In reactor S2, As(V)-O increased while As(III)-O and As(III)-S gradually decreased, likely sequestered on Fe (oxyhydr)oxides and schwertmannites regardless oxic and anoxic conditions. Finally, in the reactor 3, microbial sulfate reduction led to the dissolved As immobilization via reduction of soluble As compounds (e.g., thioarsenic) with pyrite (FeS_2) (Figure 11)

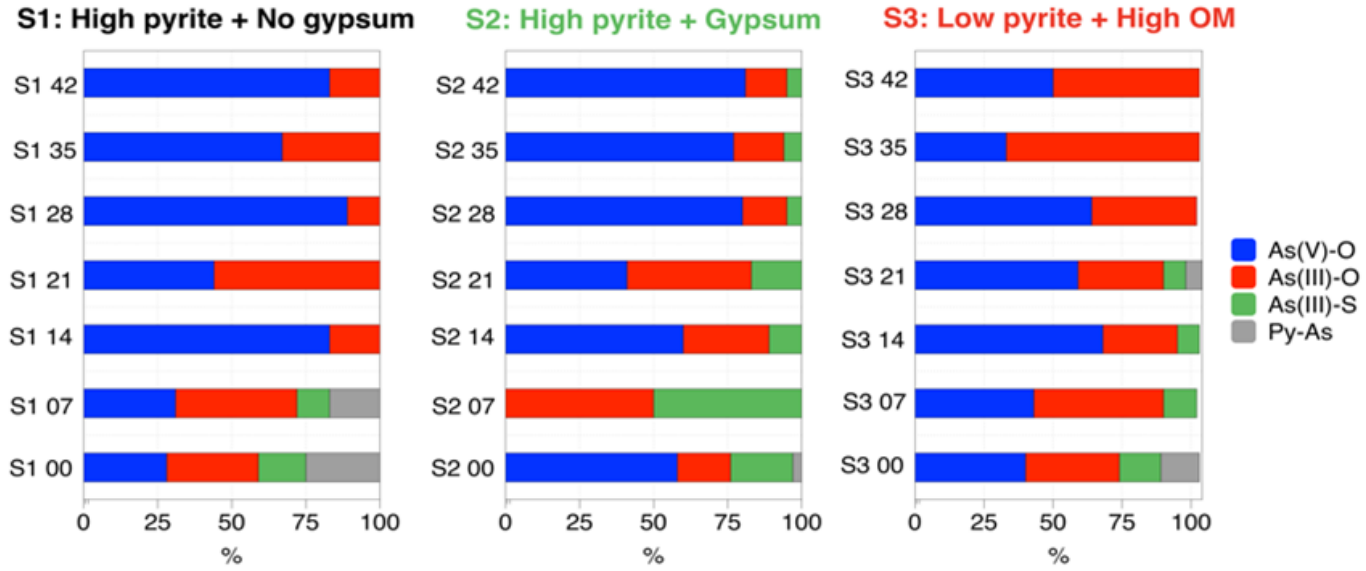

Figure 11 Associated histograms present the contributions of each As species in the sediment samples normalized to 100% in S1, S2, S3 following the redox oscillations.

Publications: [Sci. Total Environ. **663 (2019)**, 718-730; Geosci. Front. **10 (2019)**, 1715-1729.]

Hybrid Au/CuO Nanoparticles: Effect of Structural Features for Selective Benzyl Alcohol Oxidation

M. Marelli [1], A. Jouve [1,2], A. Villa[1,2], R. Psaro[1], A. Balerna[3], L. Prati[1,2], C. Evangelisti[1]

[1]CNR-ISTM Milan, [2]University of Milan, [3]INFN-LNF

Bimetallic nanoparticles (NPs) have received great interest over the last decade owing to their unique catalytic features. The design of bimetallic NPs by advanced synthetic approaches offers an effective way to control their size, shape, composition, and crystal structure which in turn are able to fine-tune their physicochemical properties. Among the promising metal pairs, Au/Cu NPs as alloys or core-shell structures have been investigated pointing out at times a positive beneficial effect in terms of catalytic performances and stability with respect to their monometallic counterparts [1]. Recently, in order to disclose the essence of the synergistic effect between gold and copper in oxidation reactions, the structural evolution of supported Au/Cu alloy NPs in the CO oxidation reaction has been deeply investigated by different research groups [2]. Despite experimental and theoretical efforts, the control of copper surface segregation (i.e., the thickness of CuO on the surface) in Au/Cu alloy NPs under oxidative conditions and thus their behavior in catalytic oxidations is still a challenge. As a matter of fact, the degree of phase segregation is strongly influenced by the reaction conditions and oxidative/reductive pretreatments, the substrates/metals interaction, the particle metal ratio, and the synthetic approach.

Hybrid Au/CuO NPs supported on carbon by solvated metal atom dispersion (SMAD) with different Au/Cu molar ratios (i.e., 13/1, 4/1, 1/1, and 1/17) for selective liquid-phase oxidation of benzyl alcohol to benzaldehyde were synthetized [3]. The morphological and structural features of the SMAD-derived AuCu bimetallic catalysts containing different Au/Cu molar ratios were investigated by high-resolution transmission electron microscopy (HRTEM), scanning transmission electron microscopy (STEM - EDS) (Figure 12 Left) and X-ray absorption fine structure (XAFS) measurements, performed at the Italian LISA CRG beamline at ESRF, disclosing the role of the local particles/structure/composition and their catalytic properties. XAFS measurements and data analyses were performed at the Cu K edge and at the Au L_3 edge to define the present Cu oxide phase and to confirm the presence of an Au core and a Cu(II)-like shell structure.

The relevant characteristics of the LISA beamline in XAFS measurements in fluorescence mode were very important especially in the study of the bimetallic sample with the very low Au and Cu contents, Au_1Cu_{17}/C and $Au_{13}Cu_1$/C (Figure 12 Right), confirming also in these cases the presence of a Cu(II)-like shell structure (complete and incomplete) around gold cores.

The catalytic behaviour of the bimetallic catalysts, evaluated in selective benzyl alcohol oxidation carried out in the liquid phase, was fundamental to explore the effect of the CuO structures on the Au-driven catalytic activity. As a result, the highest increase in the catalytic activity with respect to the monometallic Au sample was observed for the catalysts containing low Cu loading, Au_4Cu_1/C and $Au_{13}Cu_1$/C (conversion after 6 h of 97−99%). In these samples, the segregated CuO partially covered the surfaces of Au-rich cores. On the other hand, when the CuO shell wrapped the Au core completely (i.e., at high Cu loading, e.g., Au_1Cu_{17}/C), the reaction was completely inhibited.

The co-presence of Au and segregated CuO at the surface of the NPs plays a pivotal role in obtaining a beneficial synergistic effect in AuCu bimetallic catalysts for liquid-phase alcohol oxidation. Finally, the reported results can effectively contribute to fine-tune the catalytic properties of AuCu bimetallic catalysts in other chemical reactions.

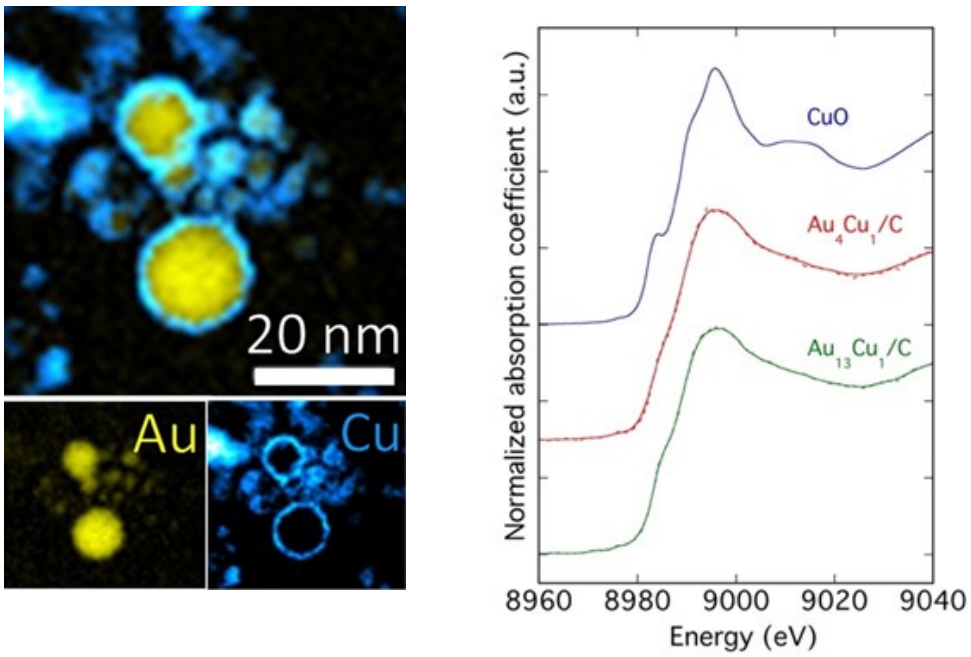

Figure 12: Left: STEM- energy filtered maps for Au and Cu of the Au1Cu17 sample (Au (2239 -2477) eV - Cu (953-1202) eV). Right: XANES spectra of the bimetallic AuCu catalysts with the lower Cu wt.% and of the CuO reference sample. For the bimetallic systems the solid lines represent the smoothed experimental data.

Publication: [J. Phys. Chem. C **123** (2019), 2864.]

References: [1] C.L. Bracey, P.R. Ellis, G.J. Hutchings Chem. Soc. Rev. **38** (2009), 2231-2243. [2] See as example: W. Zhan, J. Wang, et al, J. Am. Chem. Soc. **139** (2017), 8846−8854 [3] G M. Marelli, A. Jouve, A. Villa, R. Psaro, A. Balerna, L. Prati, C. Evangelisti, J. Phys. Chem. C **123** (2019), 2864. [4] C. Evangelisti, A. Balerna, R. Psaro, G. Fusini, A. Carpita and M. Benfatto, ChemPhysChem **18** (2017), 1.

Cu(II) binding to α synuclein fibrils

K. Paulina, D. Valensin, S. Mangani

Department of Biotechnology, Chemistry and Pharmacy University of Siena Italy

Alpha-synuclein (αS) is an intrinsically disordered protein composed of 140 amino acids, which is mainly found in the presynaptic terminals of mammalian brains. This protein is well known for its involvement in neurodegenerative disorders – Parkinson's disease (PD) and other synucleopathies. Development of PD is associated with αS aggregation into oligomers and fibrils. Metal ions and especially Cu(II) are known to accelerate fibril formation. In our studies we used XAS spectroscopy to examine the coordination sphere of Cu(II) and possible binding sites in αS fibrils. Our findings reveal some differences between coordination behavior of monomeric protein and fibrillated one and give a new insight into the interactions of Cu(II) with αS fibrils.
We investigated the XAS behavior of the three αS samples: 1. monomer αS, 2. αS fibrils formed in presence of Cu(II) (Fibril A) and 3. αS fibrils incubated with Cu(II) (Fibrils B). The obtained spectra are reported in Figure 13 A.

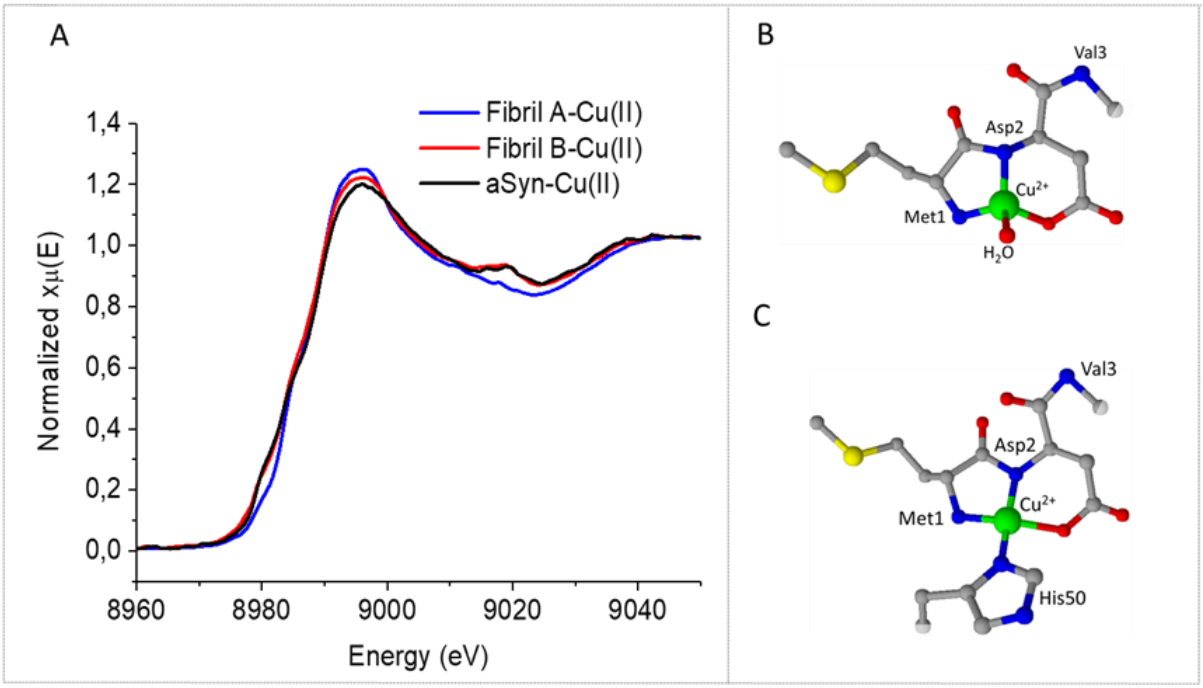

Figure 13 A. Cu K-edge XANES spectra of three samples examined: Cu(II)-AS monomeric complex, Cu (II) -"Fibril A" and Cu(II) -"Fibril B"; B. Model 2N2O, Model 3N1O.

The experimental k3 weighted EXAFS spectra and the corresponding Fourier transforms were compared with the theoretical data obtained by using either 2N2O (Figure 13 B) or 3N1O (Figure 13 C) models. For all the three analyzed system we obtain reliable fitting, as indicated by the small R-factor ranging from 0.023 to 0.011. Nevertheless, our findings reveal that model 3N1O the best fit for "Fibril A" sample, while model 2N2O fits better the "Fibril A" sample (Figure 14).

This observation suggests that αS fibrils bind Cu(II) differently according if Cu(II) is added before or after fibrils formation. In the former case Cu(II) coordinates to the peptide nitrogen atoms of Met1 and Asp2, the Nδ1 of His50 side chain and one carboxylate oxygen of Asp2. In the other fibrils sample, where the metal ions are added to the preformed fibrils, Cu(II) is bounds only to the N-terminal domain with two main chain nitrogen atoms of Met1 and Asp2, one carboxylate oxygen from Asp2 and a H_2O molecule.

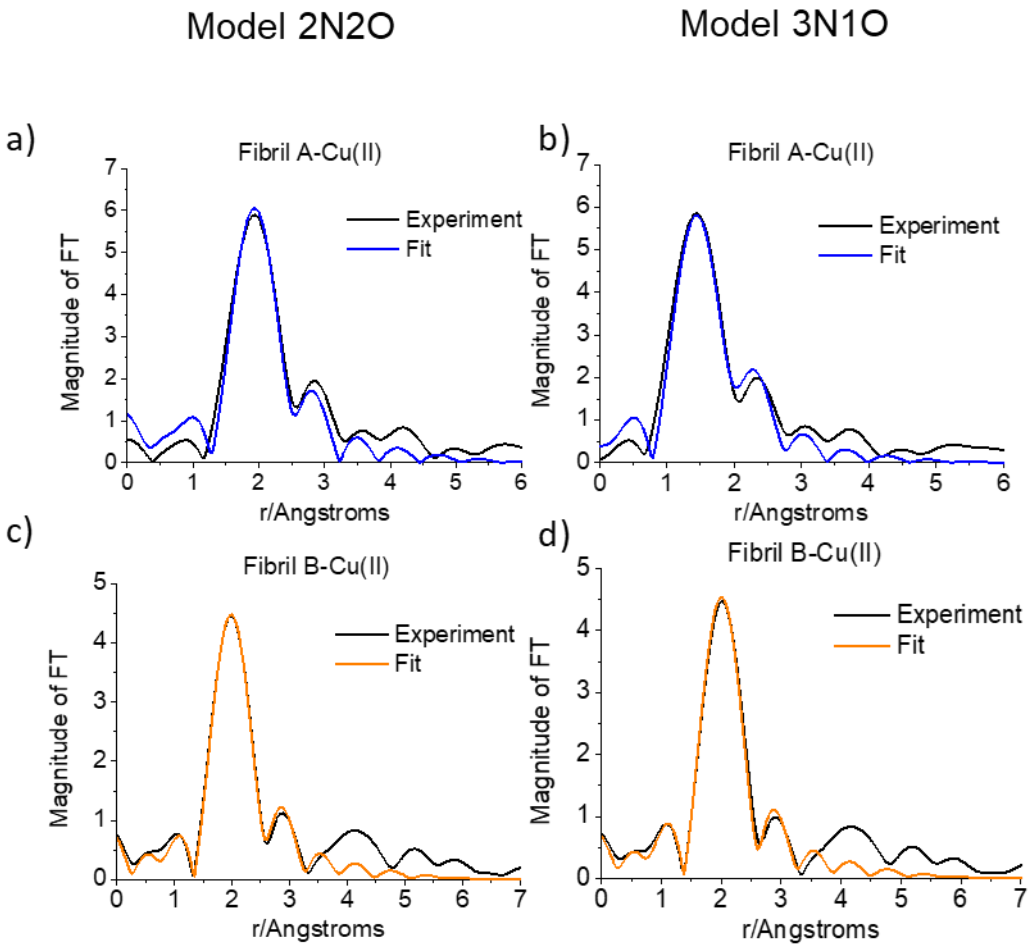

Figure 14: Experimental and simulated Fourier transforms of EXAFS spectra of "Fibril A" (a and b) and "Fibril B" (c and d) fitted for model 2N2O and for model 3N1O.

Acknowledgement: We thank Dr. Francesco d'Acapito for his helpful assistance at the LISA CRG beamline.

Publication: [Inorg. Chem. **58** (2019), 10920-10927]

1. Berretti E., Giaccherini A., Montegrossi G., d'Acapito F., Di Benedetto F., Zafferoni C., Puri A., Lepore G.O., Miller H., Giurlani W., Innocenti M., Vizza F., Lavacchi A. - In-situ quantification of nanoparticles oxidation: A fixed energy X-ray absorption approach Catalysts 9, 659-1-659-12 (2019)
2. Bloch D.N., Kolkowska P., Tessari I., Baratto M.C., Sinicropi A., Bubacco L., Mangani S., Pozzi C., Valensin D., Miller Y. - Fibrils of alpha-synuclein abolish the affinity of Cu2+-binding site to His50 and induce hopping of Cu2+ ions in the termini Inorganic Chemistry 58, 10920-10927 (2019)
3. d'Acapito F., Lepore G.O., Puri A., Laloni A., La Manna F., Dettona E., De Luisa A., Martin A. - The LISA beamline at ESRF Journal of Synchrotron Radiation 26, 551-558 (2019)
4. Di Benedetto F., Giaccherini A., Montegrossi G., Pardi L.A., Zoleo A., Capolupo F., Innocenti M., Lepore G.O., d'Acapito F., Capacci F., Poli C., Iaia T.E., Buccianti A., Romanelli M. - Chemical variability of artificial stone powders in relation to their health effects Scientific Reports 9, 6531-1-6531-13 (2019)
5. Fracchia M., Cristino V., Vertova A., Rondinini S., Caramori S., Ghigna P., Minguzzi A. - Operando X-ray absorption spectroscopy of WO3 photoanodes Electrochimica Acta 320, 134561-1-134561-9 (2019)
6. George L.L., Biagioni C., Lepore G.O., Lacalamita M., Agrosì G., Capitani G.C., Bonaccorsi E., d'Acapito F. - The speciation of thallium in (Tl,Sb,As)-rich pyrite Ore Geology Reviews 107, 364-380 (2019)
7. Giaccherini A., Baldassarre A., Donini L., Lepore G.O., Caneschi A., De Luca A., Innocenti M., Montegrossi G., Giuseppe C., Oberhauser W., Pardi L., Romanelli M., Mannini M., Di Benedetto F. - Sustainable synthesis of quaternary sulphides: The problem of the uptake of zinc in CZTS Journal of Alloys and Compounds 775, 1221-1229 (2019)
8. Giaccherini A., Cucinotta G., Martinuzzi S., Berretti E., Oberhauser W., Lavacchi A., Lepore G.O., Montegrossi G., Romanelli M., De Luca A., Innocenti M., Moggi Cecchi V., Mannini M., Buccianti A., Di Benedetto F. - Green and scalable synthesis of nanocrystalline kuramite Beilstein Journal of Nanotechnology 10, 2073-2083(2019)
9. Hafizh I., Bellotti G., Carminati M., Utica G., Gugiatti M., Balerna A., Tullio V., Lepore G.O., Borghi G., Ficorella F., Picciotto A., Zorzi N., Capsoni A., Coelli S., Bombelli L., Fiorini C. - Characterization of ARDESIA: A 4-channel SDD X-ray spectrometer for synchrotron measurements at high count rates Journal of Instrumentation 14, P06027-1-06027-14 (2019)
10. Haubold E., Schöppe P., Eckner S., Lehmann S., Colantoni I., d'Acapito F., Di Benedetto F., Schorr S., Schnohr C.S. - Short-range versus long-range structure in Cu(In,Ga)Se2, Cu (In,Ga)3Se5, and Cu(In,Ga)5Se8 Journal of Alloys and Compounds 774, 803-812 (2019)

11. Kumar A., Naumenko D., Rossi G., Magnano E., Nappini S., Bondino F., Segoloni E., Amidani L., d'Acapito F., Boscherini F., Barba L., Pace E., Benfatto M., Casassa S., Pedio M. - The effect of long-range order on intermolecular interactions in organic semiconductors: Zinc octaethyl porphyrin molecular thin film model systems Physical Chemistry - Chemical Physics 21, 22966-22975 (2019)

12. Macis S., Rezvani J., Davoli I., Cibin G., Spataro B., Scifo J., Faillace L., Marcelli A. - Structural evolution of MoO3 thin films deposited on copper substrates upon annealing: An x-ray absorption spectroscopy study Condensed Matter 4, 41-1-41-7 (2019)

13. Maggi V., Xiao C., Marcelli A. - Condensed matter researches in cryospheric science Condensed Matter 4, 68-1-68-5 (2019)

14. Marelli M., Jouve A., Villa A., Psaro R., Balerna A., Prati L., Evangelisti C. - Hybrid Au/CuO nanoparticles: Effect of structural features for selective benzyl alcohol oxidation Journal of Physical Chemistry C 123, 2864-2871 (2019)

15. Menushenkov, A. P., V. V. Popov, B. R. Gaynanov, A. A. Ivanov, A. V. Kuznetsov, A. A. Yaroslavtsev, F. d'Acapito, and A. Puri. "Local Disorder in Ln 2 Ti 2 O 7 (Ln= Gd, Tb, Dy) Pyrochlores." JETP Letters 109, no. 8 (2019): 529-535.

16. Niedermaier M., Schwab T., Dolcet P., Bernardi J., Gross S., Bockstedte M., Diwald O. - Cobalt and iron ions in MgO nanocrystals: Should they stay or should they go Journal of Physical Chemistry C 123, 25991-26004(2019)

17. Petroselli C., Moroni B., Crocchianti S., Selvaggi R., Vivani R., Soggia F., Grotti M., d'Acapito F., Cappelletti D. - Iron speciation of natural and anthropogenic dust by spectroscopic and chemical methods Atmosphere 10, 8-1-8-15 (2019)

18. Phan V.T.H., Bardelli F., Le Pape P., Couture R., Fernández-Martínez A., Tisserand D., Bernier-Latmani R., Charlet L. - Interplay of S and As in Mekong Delta sediments during redox oscillations Geoscience Frontiers 10, 1715-1729 (2019)

19. Phan V.T.H., Bernier-Latmani R., Tisserand D., Bardelli F., Le Pape P., Frutschi M., Géhin A., Couture R.M., Charlet L. - As release under the microbial sulfate reduction during redox oscillations in the upper Mekong delta aquifers, Vietnam: A mechanistic study Science of the Total Environment 663, 718-730 (2019)

20. Pittarello L., Goderis S., Soens B., McKibbin Seann J., Giuli G., Bariselli F., Dias B., Helber B., Lepore Giovanni O., Vanhaecke F., Koeberl C., Magin T.E., Claeys P. - Meteoroid atmospheric entry investigated with plasma flow experiments: Petrography and geochemistry of the recovered material Icarus 331, 170-178 (2019)

21. Popov, V. V., A. P. Menushenkov, A. A. Ivanov, A. A. Yastrebtsev, B. R. Gaynanov, F. d'Acapito, and A. Puri. "A XAFS investigation of amorphous-to-crystalline and fluorite-to-pyrochlore phase transitions in Ln2M2O7 (Ln= Gd, Tb, Dy; M= Ti, Zr)." Radiation Physics and Chemistry (2019): 108469.

22. Popov, V. V., A. P. Menushenkov, A. A. Ivanov, B. R. Gaynanov, A. A. Yastrebtsev, F. d'Acapito, A. Puri et al. "Comparative analysis of long-and short-range structures features in titanates Ln2Ti2O7 and zirconates Ln2Zr2O7 (Ln= Gd, Tb, Dy) upon the crystallization process." Journal of Physics and Chemistry of Solids 130 (2019): 144-153.

23. Pugliese G.M., Stramaglia F., Goto Y., Terashima K., Simonelli L., Fujiwara H., Puri A., Marini C., Hacisalihoglu M.Y., d'Acapito F., Yokoya T., Mizokawa T., Mizuguchi Y., Saini N.L. - Temperature dependent local atomic displacements in NaSn2As2 system Journal of Physics Condensed Matter 31, 425402-1-425402-6(2019)

24. Puri A., Lepore G.O., d'Acapito F. - The new beamline LISA at ESRF: Performances and perspectives for earth and environmental sciences Condensed Matter 4, 12-1-12-7 (2019)

25. Rezvani S.J., Mijiti Y., Gunnella R., Nobili F., Trapananti A., Minicucci M., Ciambezi M., Bresser D., Nannarone S., Passerini S., Di Cicco A. - Structure rearrangements induced by lithium insertion in metal alloying oxide mixed spinel structure studied by x-ray absorption near-edge spectroscopy. Journal of Physics and Chemistry of Solids 136, 109172 -1-109172-8 (2020)

26. Rochette, Pierre, Natalia S. Bezaeva, Andrei Kosterov, Jérôme Gattacceca, Victor L. Masaitis, Dmitry D. Badyukov, Gabriele Giuli, Giovani Orazio Lepore, and Pierre Beck. "Magnetic properties and redox state of impact glasses: A review and new case studies from Siberia." Geosciences 9, no. 5 (2019): 225.

27. Sáez-Ferre S., Lopes C.W., Simancas J., Vidal-Moya A., Blasco T., Agostini G., Mínguez Espallargas G., Jordá J.L., Rey F., Oña-Burgos P., Use of Alkylarsonium Directing Agents for the Synthesis and Study of Zeolites, Chem. Eur. J. 25 (2019).

28. Schmidt N.Y., Laureti S., Radu F., Ryll H., Luo C., d'Acapito F., Tripathi S., Goering E., Weller D., Albrecht M. - Structural and magnetic properties of FePt-Tb alloy thin films Physical Review B 100, 064428-1-064428-9 (2019)

29. Vanni M., Serrano-Ruiz M., Telesio F., Heun S., Banchelli M., Matteini P., Mio A., Nicotra G., Spinella C., Caporali S., Giaccherini A., d'Acapito F., Caporali M., Peruzzini M. - Black phosphorus/palladium nanohybrid: Unraveling the nature of P–Pd interaction and application in selective hydrogenation Chemistry of Materials 31, 5075-5080 (2019)

5. Contacts

Beamline responsible:	Francesco d'Acapito dacapito@esrf.fr +33 4 7688 2426 , +33 6 8936 4302
Beamline scientist:	Alessandro Puri puri@esrf.fr +33 4 7688 2859
Local Contact:	+33 6 8838 6994
Beamline:	+33 4 7688 2085
Laboratory:	+33 4 7688 2743
Skype:	gilda_beamline
Administration:	Fabrizio La Manna lamanna@esrf.fr +33 4 7688 2962
Web page:	http://www.esrf.eu/UsersAndScience/Experiments/CRG/BM08/

Forthcoming proposals submission deadlines

ESRF quota: March 2nd 2020.

CRG quota: to be defined

6. Contributors to this issue

F. d'Acapito, A. Puri, G. O. Lepore (CNR-IOM, Grenoble), R. De Donatis (CNR-NANO, Genova), A. Balerna (LNF-INFN, Frascati), F. Bardelli (CNR-Nanotec, Roma), Van T.H. Phan (UGA, Grenoble), F. di Benedetto (Univ, Firenze) , M. Fracchia (Univ. Pavia), D. Valensin, S. Mangani (Univ. Siena), P. Noé (CEA-LETI, Grenoble), M. Vanni (CNR-ICCOM, Sesto Fiorentino).